

Chemical abundances in the outskirts of nearby galaxy groups measured with joint *Suzaku* and *Chandra* observations

Arnab Sarkar,^{1,2*}  Yuanyuan Su,¹ Nhut Truong,³ Scott Randall,²  François Mernier,^{4,5} 

Fabio Gastaldello,⁶  Veronica Biffi,⁷ and Ralph Kraft.² 

¹Physics and Astronomy, University of Kentucky, 505 Rose street, Lexington, KY 40506, USA

²Center for Astrophysics | Harvard & Smithsonian, 60 Garden Street, Cambridge, MA 02138, USA

³Max-Planck-Institut für Astronomie, Königstuhl 17, D-69117 Heidelberg, Germany

⁴European Space Agency (ESA), European Space Research and Technology Centre (ESTEC), Keplerlaan 1, 2201 AZ Noordwijk, The Netherlands

⁵SRON Netherlands Institute for Space Research, Sorbonnelaan 2, NL-3584 CA Utrecht, The Netherlands

⁶Instituto di Astrofisica Spaziale e Fisica Cosmica (INAF-IASF), Milano, via A. Corti 12, I-20133 Milano, Italy

⁷INAF — Osservatorio Astronomico di Trieste, via Tiepolo 11, I-34143 Trieste, Italy

Accepted XXX. Received YYY; in original form ZZZ

ABSTRACT

We report results from deep *Suzaku* and mostly snapshot *Chandra* observations of four nearby galaxy groups: MKW4, Antlia, RXJ1159+5531, and ESO3060170. Their peak temperatures vary over 2–3 keV, making them the smallest systems with gas properties constrained to their viral radii. The average Fe abundance in the outskirts ($R > 0.25R_{200}$) of their intragroup medium (IGrM) is $Z_{\text{Fe}} = 0.309 \pm 0.018 Z_{\odot}$ with $\chi^2 = 14$ for 12 degrees of freedom, which is remarkably uniform and strikingly similar to that of massive galaxy clusters, and is fully consistent with the numerical predictions from the IllustrisTNG cosmological simulation. Our results support an early-enrichment scenario among galactic systems over an order of magnitude in mass, even before their formation. When integrated out to R_{200} , we start to see a tension between the measured Fe content in ICM and what is expected from supernovae yields. We further constrain their O, Mg, Si, S, and Ni abundances. The abundance ratios of those elements relative to Fe are consistent with the predictions (if available) from IllustrisTNG. Their Type Ia supernovae fraction varies between 14%–21%. A pure core collapsed supernovae enrichment at group outskirts can be ruled out. Their cumulative iron-mass-to-light ratios within R_{200} are half that of the Perseus cluster, which may imply that galaxy groups do not retain all of their enriched gas due to their shallower gravitational potential wells, or that groups and clusters may have different star formation histories.

Key words: X-rays: galaxies: clusters – galaxies: clusters: intracluster medium

1 INTRODUCTION

Big Bang nucleosynthesis primarily produced all the hydrogen and helium in the Universe, and trace amounts of a few lighter elements like Li and Be. Heavier elements are later forged in stars. Clusters of galaxies, with their deep gravitational potential wells, retain substantial X-ray emitting hot gas ($T \sim 10^7$ – 10^8 K), the so-called intracluster medium (ICM) (Ettori & Fabian 1999). A dominant fraction of metals in the local Universe can be found in the ICM, making them a unique astrophysical laboratory to probe nucleosynthesis and the chemical enrichment history of the Universe (Biffi et al. 2018a; Mernier et al. 2018a).

The enrichment processes in the ICM remain an open question. In the late enrichment scenarios (after the cluster is assembled), the ICM metal distributions are expected to be non-uniform, with a significant amount of azimuthal scatters (Domainko et al. 2006). For instance,

galactic materials can be stripped off the galaxies and deposited in the ICM as the infalling galaxies interact with the dense gas (e.g., Gunn & Gott 1972; Fabjan et al. 2010), which enriches the ICM along the directions of infalling galaxies. Also, the metals dispersed into the ICM at later times should broadly follow the spatial distributions of galaxies, leading to flat metal mass-to-light ratios (Matsushita et al. 2013). Neither of these is consistent with the observations. Nearby massive clusters, such as Perseus, show a remarkably homogeneous Fe abundance of $\sim 0.3 Z_{\odot}$ at $R > 0.25R_{200}$ [†] (Urban et al. 2017; Werner et al. 2013). Previous studies, using *Chandra*, *Suzaku*, and *XMM-Newton* observations, have reported steep iron mass-to-light ratios (IMLRs) for several galaxy clusters out to 0.2–0.5 R_{200} (e.g., Matsushita et al. 2007; Sato et al. 2009; Simionescu et al. 2011), which indicates that metal mass is more extended than the distribution of cluster galaxies. Although the ICM can achieve a uniform distribution of metals in the late enrichment process via large-scale

* E-mail: arnab.sarkar@uky.edu, arnab.sarkar@cfa.harvard.edu

[†] R_{Δ} the radius from within which the average matter density is Δ times the critical density of the Universe.

sloshing motion, the steep entropy profiles of galaxy clusters may prevent the efficient mixing up of metals across the large radii (Do-mainko et al. 2006; Werner et al. 2013; Ghizzardi et al. 2014).

The observed uniform Fe abundances and steep IMLR profiles suggest an early enrichment scenario, in which most of the enrichment occurred in the proto-cluster environment (e.g., Fabjan et al. 2010; Biffi et al. 2017). This process is primarily driven by the galactic winds and active galactic nuclei (AGN) feedback at the epoch of the peak star formation (around $z \sim 2-3$; Madau & Dickinson 2014). The strong galactic winds and AGN activity may have expelled much of the metals from the interstellar medium (ISM) and uniformly mixed the intergalactic gas even before the cluster was assembled.

With a better understanding of stellar nucleosynthesis over the past decades, it is now evident that most of the lighter elements, like O, Mg, and Ne, are synthesized by massive stars and expelled into the ICM by core-collapsed supernovae (SNcc) (e.g., Nomoto et al. 2006), while the heavier elements, like Ar, Ca, Fe, and Ni, are primarily produced by Type Ia supernovae (SNe Ia) (e.g., Iwamoto et al. 1999; Sarkar et al. 2021b). Elements such as Si and S are produced relatively comparably by SNe Ia and SNcc (e.g., de Plaa et al. 2007). Therefore, the metal abundance pattern of heavier elements strongly depends on the SNe Ia explosion mechanism, and the abundances of lighter elements depend on the stellar initial mass function (IMF) of galaxies (Mernier et al. 2015, 2016b). The measurement of the abundance profiles of those metals is crucial to constrain supernovae models, and to probe the chemical enrichment history of the ICM.

The α -capture (such as O, Mg, Ne, Si, S) and Fe peak elements (such as Cr, Mn, Fe, Co, Ni) can be observed from their emission lines in X-ray. Most of these emission lines originate from the K and L – shell transitions in highly ionized plasma (Chakraborty et al. 2020a,b). Since the ICM is very close to collisional ionization equilibrium and optically thin, the equivalent widths of those emission lines can easily be converted to element abundances (Böhringer & Werner 2010; Mernier et al. 2016a; Urban et al. 2017). Using *Chandra* observations, Rasmussen & Ponman (2007) have found that the Si/Fe ratio increases with radius, strongly suggesting an excess of SNe Ia contribution at the cluster center, while the SNcc contribution dominates at the outskirts. Later on, however, it was observed in M87 that the Si abundance profile is even more centrally peaked than Fe (Million et al. 2011). Most recently, an extensive *Suzaku* investigation of the nearby Virgo cluster reveals an SNIa fraction of 12–37% throughout its ICM, which challenges pure SNcc enrichment at the cluster outskirts (Simionescu et al. 2015). The current view is that abundance profile is roughly the same for all elements.

The enrichment process in lower mass systems (groups) is even less straightforward (Gastaldello et al. 2021). With deep gravitational potential wells, galaxy clusters behave like closed-box systems, holding all of the metals ever produced by the stars inside their virial radius (e.g., de Plaa et al. 2007). In contrast, galaxy groups have shallow gravitational potential wells, which makes them more vulnerable to losing material via non-gravitational processes, such as galactic winds driven by supernovae (SNe) and AGN feedback (e.g., Rasmussen & Ponman 2007; Lovisari et al. 2015; Thölken et al. 2016). These processes may expel much of the enriched gas out of the system (Sarkar et al. 2021a). Using *ASCA* data, Makishima et al. (2001) found that the IMLRs in galaxy groups within $0.5 R_{200}$ increase with their masses, while those of galaxy clusters are not mass-dependent, and are systematically higher than groups. The metal budgets out

Table 1. Observational log

Name	Obs Id	Obs Date	Exp. (ks)
<i>Suzaku</i>			
MKW4 central	808066010	2013 Dec 30	34.6
MKW4 Offset 1	805081010	2010 Nov 30	77.23
MKW4 N2	808067010	2010 Nov 30	97
MKW4 Offset 2	805082010	2010 Nov 30	80
MKW4 E1	808065010	2013 Dec 29	100
MKW4 NE	809062010	2013 Dec 29	87.5
Antlia E0	802035010	2007 Nov 19	55
Antlia E1	807066010	2012 Jun 13	20
Antlia E2	807067010	2012 Jun 14	21
Antlia E3	807068010	2012 Jun 15	19
Antlia E4	807069010	2012 Jun 16	17
Antlia E5	807070010	2012 Jun 17	39
Antlia EB	807071010	2012 Jun 18	38
RXJ1159 N	804051010	2009 May 02	84
RXJ1159 S	807064010	2012 May 27	81
	807064020	2012 Dec 18	21
RXJ1159 E	809063010	2014 May 29	96
RXJ1159 W	809064010	2014 May 31	94
ESO3060170 central	805075010	2010 May	27
ESO3060170 offset	805075060	2010 May	70
<i>Chandra</i>			
MKW4 central	3234	2002 Nov 24	30
MKW4 N2	20593	2019 Feb 25	14
MKW4 E1	20592	2018 Nov 17	15
MKW4 NE	20591	2019 Mar 08	14
Antlia E1	15090	2013 Nov 20	7
Antlia E2	15089	2013 Nov 22	7
Antlia E3	15088	2013 Jul 02	7
Antlia E4	15086	2013 Nov 04	7
Antlia E5	15085	2013 Apr 05	7
Antlia EB	15087	2013 Nov 04	7
RXJ1159 central	4964	2004 Feb 11	76
RXJ1159 NW	14026	2012 Aug 09	50
RXJ1159 NE	14473	2012 Aug 12	37
	14027	2012 Aug 09	13
ESO3060170 central	3188	2002 March 08	14.06
ESO3060170 offset	17219	2015 Oct 09	9.84

to the virial radius of groups are relatively unexplored, due to their low surface brightness. The emission from the outskirts of groups is typically dominated by the X-ray background, which makes the measurement of metal abundances very challenging (Rasmussen & Ponman 2009). With its stable particle background and higher spectral sensitivity below 1 keV (Koyama et al. 2007), *Suzaku* can measure the metal abundances more precisely at R_{200} and beyond. The inclusion of snapshot *Chandra* observations resolves much of the Cosmic X-ray Background (CXB), which is crucial to pin down the systematic uncertainty.

In this paper, we study the metal abundances of four galaxy groups: MKW4, Antlia, RXJ1159+5531 (hereafter RXJ1159), and ESO3060170, from their centers out to R_{200} , with *Suzaku* and *Chandra*. Their peak temperatures (just outside the group core at $\sim 0.25 R_{200}$) are 2.2 keV, 2.3 keV, 2.5 keV, and 2.7 keV, respectively. To our knowledge, they are the lowest mass systems with their gas properties constrained at R_{200} . MKW4, RXJ1159, and ESO3060170 are cool core systems, while Antlia is a non-cool-core group. The thermodynamic properties of these four galaxy groups out to their virial radii are reported in Sarkar et al. (2021a), Wong et al. (2016),

Table 2. Properties of the groups

Name	peak temp (keV)	R ₂₀₀ (kpc)	z	scale (1'') (kpc)	CC/NCC
MKW4	2.2	884	0.02	0.443	CC
Antlia	2.3	887	0.009	0.213	NCC
RXJ1159	2.5	871	0.081	1.583	CC
ESO3060170	2.7	1150	0.0358	0.73	CC

Su et al. (2015), and Su et al. (2013), respectively. Unlike massive galaxy clusters, these groups do not show obvious flattening of their entropy profiles at large radii. We use NASA/IPAC Extragalactic Database[‡] to estimate the luminosity distance for MKW4, Antlia, RXJ1159, and ESO3060170, by adopting a cosmology of $H_0 = 70 \text{ km s}^{-1} \text{ Mpc}^{-1}$, $\Omega_\Lambda = 0.7$, and $\Omega_m = 0.3$. Table 2 outlines the physical properties of our four groups. Throughout this paper, we assume a solar abundance table of Asplund et al. (2009). All uncertainties are reported at a 68% confidence level.

2 OBSERVATIONS AND SPECTRAL ANALYSIS

MKW4 has been observed out to the virial radius with *Suzaku* and *Chandra* in three directions (north, east, and northeast). Antlia and ESO3060170 have each been mapped to the virial radius in one direction, east and south, respectively. RXJ1159 has been observed to the virial radius with full azimuthal coverage. The detailed observations are listed in Table 1. The exposure corrected and background subtracted mosaic *Suzaku* images of four groups in the 0.5–2.0 keV energy band are shown in Figures A1, A2, A3, and A4, respectively. We followed the data reduction procedure described in Sarkar et al. (2021a) for MKW4, Wong et al. (2016) for Antlia, Su et al. (2015) for RXJ1159, and Su et al. (2013) for ESO3060170. In short, we extracted spectra from several annular regions, from the center out to the virial radius of each group, as marked in green annular sectors in Figures A1, A2, A3, and A4. We generated redistribution matrix files (RMF) and instrumental background files (NXB) for all regions and detectors. For each region, one ancillary response file (ARF) was generated using a β -profile image to model the ICM component; another ARF was produced for a uniform emission in a circular region of 20' radius to model the sky X-ray background.

Spectral analysis was performed using XSPEC-12.10.1 and Cash statistics (Cash 1979). We fit the spectra extracted from XIS0, XIS1, and XIS3 simultaneously. For MKW4, the spectral fitting was restricted to the energy range of 0.4 - 7 keV for XIS1 and 0.6 - 7 keV for XIS0 and XIS3 (Sarkar et al. 2021a), while the energy range of 0.5-7 keV was used for the other three groups. We fit each spectrum with a multi-component X-ray background model and a thermal emission model. For the X-ray background model, we adopted $\text{phabs}(\text{pow}_{\text{resolvedCXB}} + \text{pow}_{\text{unresolvedCXB}} + \text{apec}_{\text{MW}}) + \text{apec}_{\text{LHB}}$. The $\text{pow}_{\text{resolvedCXB}}$ component represents the point sources resolved by *Chandra*[§]. A mosaic image of *Chandra* observations of each

group in the 0.5–7.0 keV energy band is shown in Figures A1, A2, A3, and A4, with all resolved point sources marked with green elliptical regions. The second power-law component ($\text{pow}_{\text{unresolvedCXB}}$) describes the unresolved point sources. The two thermal apec components model the foreground emissions from Milky Way (apec_{MW}) and Local Hot Bubble (apec_{LHB}).

Two thermal components associated with a photoelectric absorption component - $\text{phabs} \times (\text{vpec} + \text{vpec})$ were fitted to the spectra of each group to model the ICM emission from each annulus^{*}. The galactic hydrogen column densities in the directions of MKW4, Antlia, RXJ1159, and ESO3060170 were obtained using the HEASARC N_{H} tool[¶]. We link the temperature of the cooler component of each region to half that of the hotter component. The normalizations of both components are allowed to vary freely. The best-fit spectral models for the outermost regions of the four groups are shown in Figure A5.

For MKW4 and Antlia, we simultaneously fit spectra from regions in different azimuthal directions. We let the temperatures and normalizations vary freely among different regions while linking the abundances of regions at the same distance from the group center. We allow the abundances of O, Mg, Si, S, Fe, and Ni to vary freely, while the rest of the elements were varied collectively. The abundances of Ar and Ca were linked to S. We are unable to constrain the S abundance for E2 and E3 pointings of Antlia. We, therefore, fixed the Si abundance to be equal to the S abundance. For the outer three regions of MKW4 at R₂₀₀, and the outer two regions of Antlia at R₂₀₀ (E4 and E5), we did not find any good constraint on their metal abundances when fitted individually. Therefore, we performed a simultaneous fitting for all those 5 regions. Their temperatures and normalizations were allowed to vary freely, but with their metallicities linked. The virial temperatures of MKW4 and Antlia are nearly the same. Both groups display entropy profiles rising to R₂₀₀. The distance of MKW4 is twice that of Antlia, which makes the outermost regions of MKW4 (R = 706-1200 kpc) cover almost the same physical radial range as the outermost two regions in Antlia (R = 828-1302 kpc). It is, therefore, reasonable to assume that they have similar metallicities at R₂₀₀.

For RXJ1159 and ESO3060170, we set their Ni abundance to 1 Z_\odot (the best fit for MKW4 and Antlia), as we could not find a good constraint when letting it vary freely. The remaining elements were allowed to vary as described for MKW4 and Antlia. We also find it necessary to link the abundance of region 3 to that of region 4, and the abundance of region 5 to that of region 6, for ESO3060170 (the temperature and normalization of each region are free to vary). We did not perform any deprojection during spectral fitting since it may introduce systematic noise (Nulsen & Böhringer 1995; McLaughlin 1999). The best-fit Fe, O, Mg, Si, S, and Ni profiles of each group are shown in Figures A1, A2, A3, and A4.

* The Fe abundance measurement is biased low when fitting multi-phase gas with a single temperature model (e.g., Buote & Fabian 1998; Buote 2000; Gastaldello et al. 2021). Given *Suzaku*'s modest angular resolution, each radial bin covers a sizable physical region, likely associated with temperature variation even at cluster outskirts. When fitting a single temperature spectrum generated with Xspec *fakeit* to our 2T model, no bias to the metal abundance measurement is found. Therefore, our model should not introduce any bias if even the gas is single phase.

¶ <http://heasarc.gsfc.nasa.gov/cgi-bin/Tools/w3nh/w3nh.pl>

‡ <http://ned.ipac.caltech.edu>

§ We produce synthetic *Suzaku* observations for each point source using *xissim* based on their position and flux determined by *Chandra*. We extract spectra from these synthetic *Suzaku* observations using the same extraction regions as the radial profiles. Those spectra are then fit to a powerlaw model with an index of 1.41 to obtain the normalization of $\text{pow}_{\text{resolvedCXB}}$.

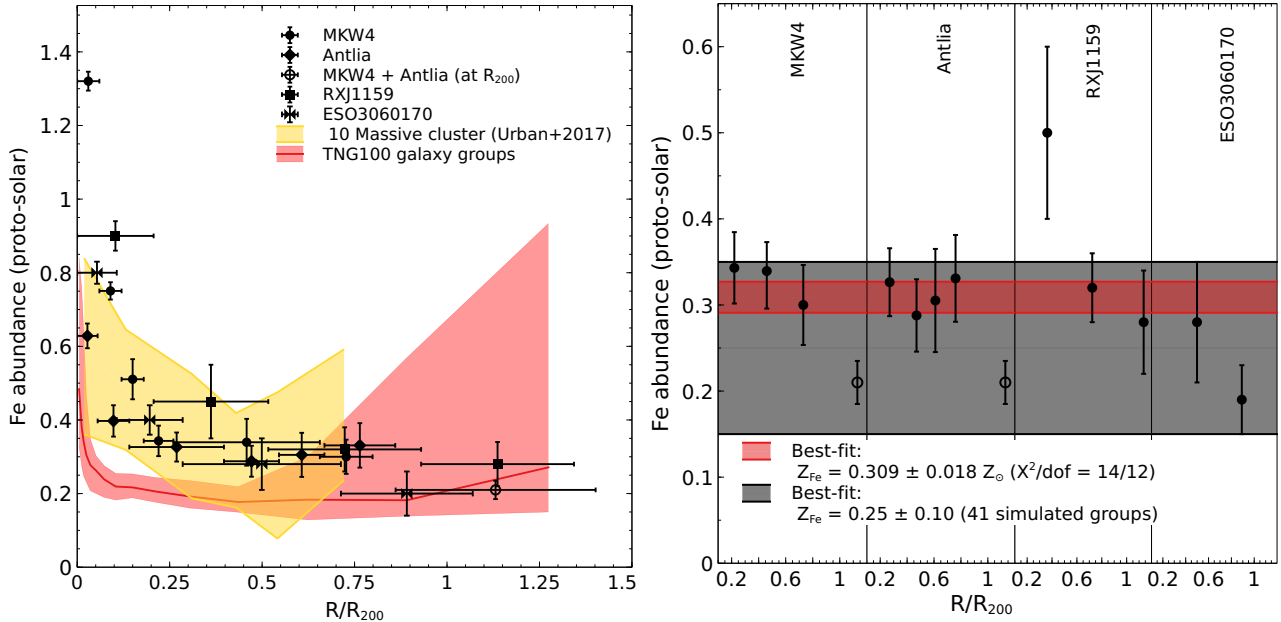


Figure 1. Left: Fe profiles obtained from the 2T vpec model. All abundances are in the solar unit. We assume a solar abundance table of [Asplund et al. \(2009\)](#). Yellow shaded region represents the measurement of Fe abundance in 10 massive clusters ([Urban et al. 2017](#)). Red shaded region shows the average Fe abundance profile with 16–84 percentile error, obtained from 41 galaxy groups in TNG100. Right: Iron abundances at $R > 0.25R_{200}$ of individual groups. The red shaded region indicates average iron abundance for $0.25-1.0R_{200}$ with 1σ uncertainty. The black shaded region represents average iron abundance at $R > 0.25R_{200}$ for 41 galaxy groups in TNG100. Open circles represent Fe abundance at R_{200} of Antlia and MKW4, measured jointly.

3 RESULTS

3.1 Fe abundance profiles

We obtain abundance profiles of Fe for four groups out to R_{200} , as shown in Figure 1 and Figures A1, A2, A3, and A4. Within $0.25R_{200}$, their Fe abundances increase towards their centers, with MKW4 showing the strongest gradient, reaching $1.3Z_{\odot}$ in the center. This may be partially due to the smaller radial bin width that has been resolved for MKW4. The Fe abundance profile of Antlia is much flatter at $R > 0.05R_{200}$, with the smallest central Fe abundance of $0.6Z_{\odot}$ at $R < 0.05R_{200}$. Unlike the other three groups, Antlia is a non-cool-core system. The mechanism that has disrupted its core, such as a major merger, may have redistributed its central metal content at $R > 0.05R_{200}$ (e.g., [Murray et al. 2018](#); [Lovisari & Reiprich 2019](#)).

Even though these systems show a variety of Fe abundances at their centers, the Fe abundance profiles start to converge outside their cores. In the outskirts, the Fe abundances are mostly consistent within uncertainties. We measure an average Fe abundance of $0.309 \pm 0.018 Z_{\odot}$ ($\chi^2 = 14$ for 12 degrees of freedom) over the radii of $0.25-1.0R_{200}$. This is strikingly similar to what was found for 10 nearby massive clusters, with a Z_{Fe} of $0.316 \pm 0.012 Z_{\odot}$ ($\chi^2 = 28.85$ for 25 degrees of freedom) over $0.25-1.0R_{200}$ ([Urban et al. 2017](#)), using the same Solar abundance table of [Asplund et al. \(2009\)](#).

We compare the measured Fe abundance at $R > 0.25R_{200}$ of our four groups with that of simulated groups, as shown in Figure 1. We use IllustrisTNG100, a simulation run in the IllustrisTNG project (e.g., [Naiman et al. 2018](#); [Springel et al. 2018](#); [Nelson et al. 2018](#); [Marinacci et al. 2018](#); [Pillepich et al. 2018](#)), to predict the Fe abundance in the outskirts of groups. The simulated volume is $(110.7$

$\text{Mpc})^3$, providing 41 simulated groups, defined as Friend-of-Friend halos within the mass range $M_{200} \sim 5 \times 10^{13} - 4 \times 10^{14} M_{\odot}$ at $z=0$. The abundance is measured within the range of $[0.25-1]R_{200}$, and is computed as an X-ray emission-weighted quantity, in which the X-ray emission of each simulated gas cell is obtained based on the gas thermodynamics, e.g., gas density, temperature, and metallicity, assuming an apec plasma model.

At $R < 0.5R_{200}$, simulations predict lower Fe abundances by a factor of ~ 2 compared to the observations. Similar discrepancies have been found by [Mernier et al. \(2018b\)](#) and [Leccardi & Molendi \(2008\)](#) while comparing the Fe abundance profiles with the hydrodynamic simulations. [Planelles et al. \(2014\)](#) argue that this discrepancy can be explained by the outdated assumptions on the SNe yields, the assumed initial mass function, the fraction of binary systems, and/or the SNe efficiency of releasing metals into the ICM ([Mernier et al. 2018b](#)). We test with two different SNIa yield models, i.e., the W7 model by [Iwamoto et al. \(1999\)](#), used in TNG simulations, and the yield model by [Badenes et al. \(2006\)](#), which best-fitted with our observations, as discussed in Section 3.4. By assuming a SNIa fraction of 23%, we find that the SNIa yield model of [Badenes et al. \(2006\)](#) produces $> 25\%$ more Fe than that of the W7 model, which partially explains the discrepancy seen in Figure 1 left. In addition, our sample is dominated by cool core systems with concentrated metallicity distributions, while the simulation sample has a more extensive diversity of group cores. Simulations show a large scatter in the Fe profile at $R > 0.5R_{200}$, as seen in Figure 1 left. This could be explained by the presence of satellites and high-density clumps at the outskirts. The average Fe abundance of simulated groups in the $0.25R_{200} < R < R_{200}$ range agrees with the observations, as shown in Figure 1 (right).

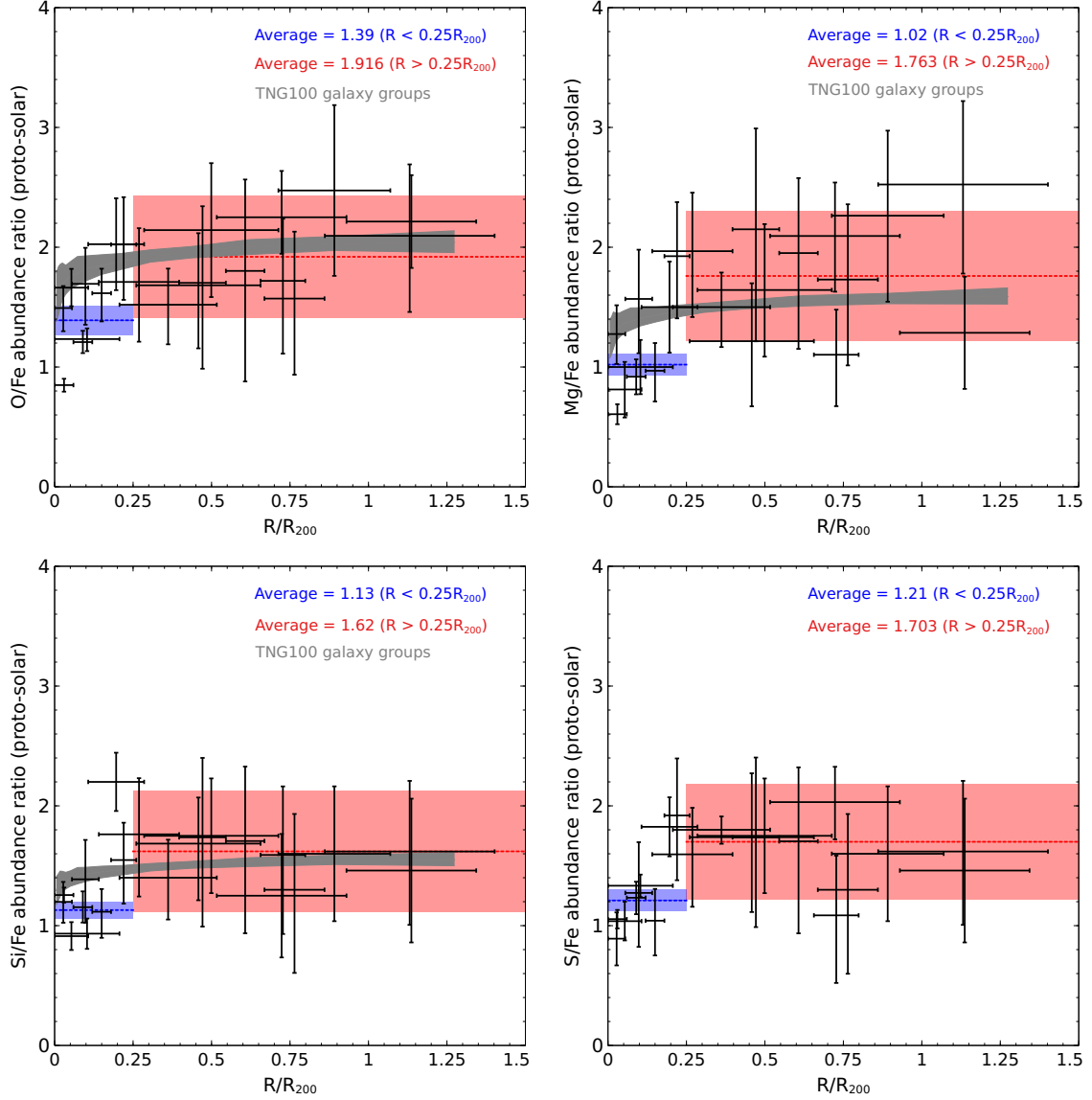


Figure 2. X/Fe ratios as a function of radius for individual metals. The red shaded region represents the average X/Fe excluding central $R < 0.25R_{200}$ region. The blue shaded region represents the average X/Fe for the central $R < 0.25R_{200}$ region. Black shaded region shows the average X/Fe profile of 41 galaxy groups in TNG100.

3.2 Chemical composition

In addition to Fe, we have further constrained the abundance profiles of O, Mg, S, Si, and Ni, as shown in Figures A1, A2, A3, and A4. We derive their abundance ratios relative to Fe as a function of radius from the centers out to the virial radii, as shown in Figure 2. The uncertainties are calculated using Monte Carlo simulations with 2000 - 3000 realizations. We observe that the X/Fe ratios are consistent with the solar abundance within $R < 0.25R_{200}$, with O/Fe = 1.39 ± 0.12 ($\chi^2/\text{degrees of freedom} = 16.7/6$), Mg/Fe = 1.02 ± 0.09 ($\chi^2/\text{degrees of freedom} = 17.6/5$), Si/Fe = 1.13 ± 0.07 ($\chi^2/\text{degrees of freedom} = 10.5/6$), S/Fe = 1.21 ± 0.09 ($\chi^2/\text{degrees of freedom} = 11.6/7$), and Ni/Fe = 1.82 ± 0.29 ($\chi^2/\text{degrees of freedom} = 16.5/4$), which is similar to what have been measured for group centers such as the CHEERS project (Mernier et al. 2018b). The X/Fe ratios over $0.25R_{200} < R < R_{200}$ are somewhat super solar with O/Fe = 1.92 ± 0.51 ($\chi^2/\text{degrees of freedom} = 5.2/12$), Mg/Fe = 1.76 ± 0.54

($\chi^2/\text{degrees of freedom} = 10/12$), Si/Fe = 1.62 ± 0.51 ($\chi^2/\text{degrees of freedom} = 8/12$), S/Fe = 1.70 ± 0.48 ($\chi^2/\text{degrees of freedom} = 6/12$), and Ni/Fe = 3.60 ± 1.50 ($\chi^2/\text{degrees of freedom} = 3.4/6$).

We compare the O/Fe, Mg/Fe, and Si/Fe ratios of our four groups with that of simulated groups, as shown in Figure 2. Since TNG simulations do not include S abundance, we could not compare the measured S/Fe ratio with the simulation. Our measured abundance ratios for O/Fe, Mg/Fe, and Si/Fe are consistent with the simulated groups within their 1σ error bars.

3.3 Iron mass-to-light ratios

We investigate the IMLR from the centers out to the virial radii of these groups to compare the Fe distribution in the IGrM with their

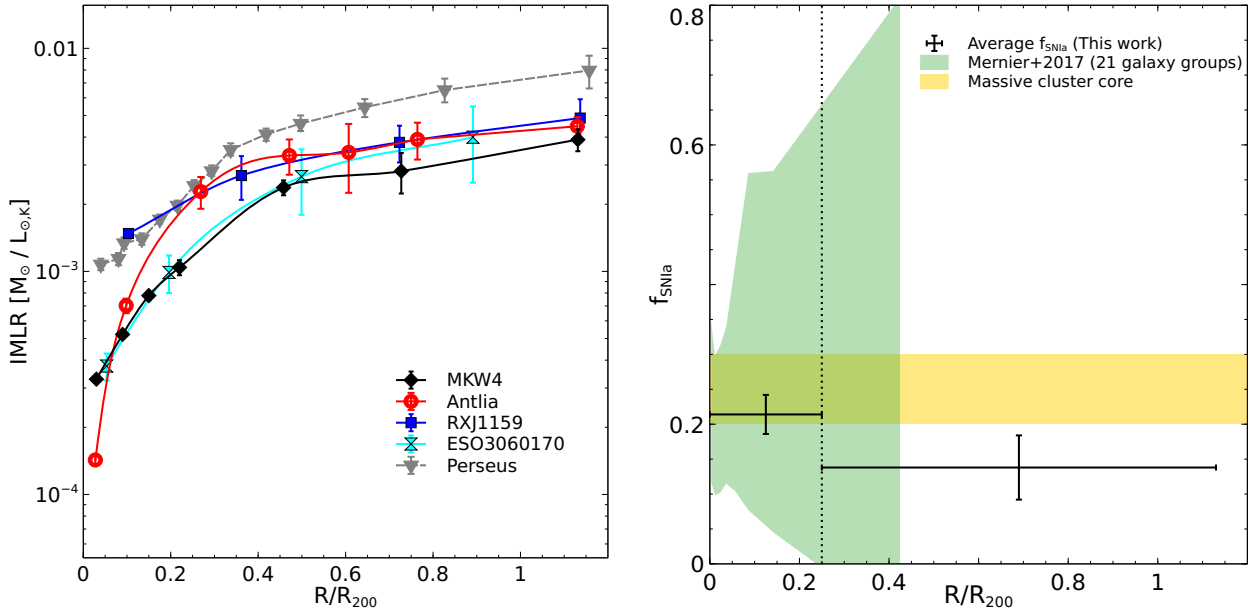


Figure 3. *Left:* Radial profiles of IMLR with K_s -band luminosity for groups in our sample and the Perseus cluster. We obtain IMLR of Perseus from Matsushita et al. (2013). *Right:* The averaged f_{SNIa} for the four groups at $R < 0.25R_{200}$ and $0.25R_{200} < R < R_{200}$. Green shaded region represents the measurement scatter obtained from a large number of groups (Mernier et al. 2017). Yellow shaded region indicates the limit of f_{SNIa} at the massive cluster core (de Plaa et al. 2007). Vertical dotted line indicates $0.25R_{200}$.

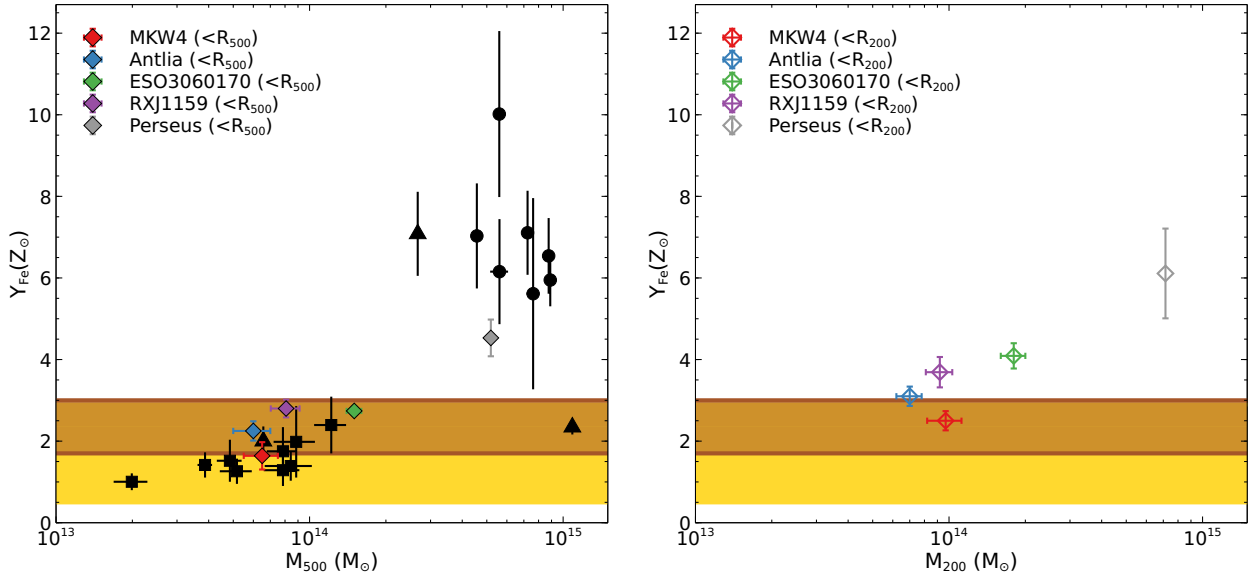


Figure 4. *Left:* Effective Fe yield as a function of cluster/group mass within R_{500} . Circles represent Fe yield for the cluster in the sample of Ghizzardi et al. (2021), squares represent the groups in the sample of Renzini & Andreon (2014), triangles represent NGC 1550, Hydra A, and Coma in the sample of Sasaki et al. (2014). Yellow shaded region shows the expected value estimated from the SN yields derived from Maoz & Graur (2017) and Renzini & Andreon (2014). The brown shaded region shows the expected value calculated assuming higher SNIa rate from Freundlich & Maoz (2021). *Right:* Effective Fe yield as a function of cluster/group mass within R_{200} .

stellar mass profiles. We use the metal abundance profiles obtained in this work, and the deprojected density profiles of MKW4, Antlia, RXJ1159, and ESO3060170 derived in Sarkar et al. (2021a), Wong et al. (2016), Su et al. (2015), and Su et al. (2013), respectively, to calculate the accumulated iron mass within a specific radius for each group. We estimate the K_s -band luminosity of each group using the

Two Micron All-Sky Survey (2MASS[‡]). We obtain a $2^{\circ} \times 2^{\circ}$ mosaic image centered at each group from the 2MASS data catalog. We adopt the Galactic extinction (A_K) values for both groups from NASA/IPAC Extragalactic Database[†]. We deproject the K_s -band luminosity with

[‡] <https://irsa.ipac.caltech.edu/applications/2MASS/IM/interactive.html>

[†] <http://ned.ipac.caltech.edu>

radius, and the resultant luminosity profiles are used to calculate the cumulative IMLR. Figure 3 shows the IMLR of MKW4, Antlia, RXJ1159, and ESO3060170 from their centers to their virial radii. Radial profiles of the IMLR increase with the radius for all groups, suggesting that their metal distribution is more extended than the galaxy light out to R_{200} . Their IMLRs within R_{500} are within the scatter of what has been found for other groups (e.g., Sato et al. 2009), although that of RXJ1159 at $0.1 R_{200}$ is exceptionally high. The IMLR profiles of these groups converge to $(4\text{--}5) \times 10^{-3} M_{\odot}/L_{K\odot}$ at R_{200} , which is half that of the Perseus cluster.

We estimate the Fe yield (Y_{Fe}), which is the ratio of total Fe mass released by stars to the total stellar mass formed for a given stellar population, as follows (Renzini & Andreon 2014; Ghizzardi et al. 2021; Gastaldello et al. 2021)

$$Y_{\text{Fe},500} = \frac{M_{\text{Fe},500}^{\text{star}} + M_{\text{Fe},500}}{M_{\text{star},500}(0)} \quad (1)$$

where $M_{\text{Fe},500}$ is the Fe mass within R_{500} , $M_{\text{Fe},500}^{\text{star}}$ is the Fe mass locked into the stars within R_{500} , $M_{\text{star},500}(0)$ is the mass of gas within R_{500} that went into stars and whose present mass is reduced by a factor r_0^{-1} , i.e., $M_{\text{star},500}(0) = r_0 M_{\text{star},500}$ (Gastaldello et al. 2021), where r_0 is the return factor. We adopt $r_0 = 1/0.58$ following Renzini & Andreon (2014) and Gastaldello et al. (2021). Figure 4 shows the effective Fe yield of four galaxy groups within R_{500} and R_{200} , respectively. We compare the Fe yield of four groups within R_{500} with the sample of clusters studied in Ghizzardi et al. (2021), the sample of groups studied in Renzini & Andreon (2014), and the systems studied in Sasaki et al. (2014). We adopt the expected values estimated by Gastaldello et al. (2021). The Fe yields within R_{200} for these four groups are significantly higher than that within R_{500} , which suggests that at the group scale feedback redistributes metals, and may push (or prevent from collapse) a consistent fraction of them out to R_{200} and beyond.

3.4 Supernovae yields

The yields of SNe Ia and SNcc are significant contributors to the metal enrichment of the ICM. We fit our measured metallicity distributions to the metallicity patterns predicted by several theoretical SNe Ia and SNcc nucleosynthesis models, following Mernier et al. (2016b). We fit the average metal abundance ratios of O/Fe, Mg/Fe, Si/Fe, and S/Fe for these groups to a combination of a single SNe Ia and a single SNcc model, and allow the relative number of SNe Ia over the total number of SNe (denoted as f_{SNIa}) free to vary (Werner et al. 2006). Mernier et al. (2016b) and Simionescu et al. (2019) pointed out that existing SNe yield models cannot successfully reproduce the observed Ni/Fe ratios, which in turn introduces significant errors in fitting parameters. We, therefore, exclude the Ni/Fe ratio from the fitting process. The α -capture elements—O and Mg are primarily produced by the SNcc, while both SNcc and SNe Ia produces Si and S. Thus, their relative abundances compared to Fe, a major SNe Ia product, are sensitive to the fitting parameters. Our measured average abundance patterns for MKW4 and Antlia fit best with the delayed detonation (DDT) SNe Ia model of Badenes et al. (2006), and with the “classical” mass-dependent SNcc model of Nomoto et al. (2006) with a progenitor metallicity of $Z_{\text{init}} = 0.02 Z_{\odot}$. For RXJ1159 and ESO3060170, we obtain a best-fit by using the SNe Ia model of

Badenes et al. (2006) and the SNcc model of Nomoto et al. (2013) and Sukhbold et al. (2016), respectively. Throughout this paper, we assume the SNcc yields are produced by the population of massive stars having a Salpeter IMF, (Salpeter 1955) with a common Z_{init} (e.g., Mernier et al. 2016b). We next fit the metal abundance patterns at each radial bin of four groups to obtain their f_{SNIa} from the centers out to the virial radii. Figure 3 shows the f_{SNIa} averaged over two radial bins, from $0 - 0.25R_{200}$ and $0.25 - 1.0R_{200}$. The derived f_{SNIa} decreases from 0.214 ± 0.028 at their centers to 0.138 ± 0.046 at the outskirts. Those values are broadly consistent with those of the core of massive galaxy clusters of 20%–30% (de Plaa et al. 2007; Simionescu et al. 2009) and our Milky Way of 15% (Tsujiimoto et al. 1995). We note that the SNe yields constitute a crucial source of bias in the above analysis. The SNe yield models suffer from uncertainties up to a factor of 2 (e.g., Wiersma et al. 2009), and as a consequence, the derived estimation of f_{SNIa} should be interpreted with caution (e.g., de Grandi & Molendi 2009; Mernier et al. 2018b).

4 SYSTEMATIC UNCERTAINTIES

We test our results against possible systematic uncertainties introduced during spectral analysis, following Sarkar et al. (2021a). One of the most critical and uncertain components of the X-ray background is the CXB. To examine the systematic uncertainty associated with the CXB, we vary the normalization of the unresolved CXB component by 10%, with a fixed power-law slope of $\Gamma = 1.41$. We obtain that the associated impacts on all the metal abundances are within the statistical error limit. Next, we estimate the systematic uncertainties introduced by the two foreground components—MW and LHB. We vary their best-fit normalizations by 10%, which does not significantly change the measured metal abundances. Finally, we experiment with a 20% variation in Galactic column density (N_{H}), which also has no significant impact on the measured metal abundances.

5 DISCUSSION

Using joint *Suzaku* and *Chandra* observations, we derived the abundance profiles of Fe, O, Mg, S, Si, and Ni for four nearby galaxy groups, from their centers out to their virial radii. To our knowledge, this is the first time that such measurements have been made for such low-mass systems. In the previous section, we show that our results are stable against various sources of systematic uncertainties. Below we compare the results with what we know from massive galaxy clusters, and discuss the implications of our findings.

5.1 Early enrichment scenario

Previous studies have reported a universal Fe abundance of $\sim 0.3 Z_{\odot}$ at the outskirts of nearby massive clusters using *Suzaku* observations (e.g., Werner et al. 2013; Urban et al. 2017). It has also been shown that no significant redshift evolution of the global metallicity ($R < R_{500}$) is found for high-redshift samples (e.g., McDonald et al. 2016; Mantz et al. 2017; Liu et al. 2020). These findings point to an early-enrichment scenario, where the ICM is enriched during the

star formation peak at $z = 2 - 3$, before the formation of galaxy clusters. The state-of-the-art hydrodynamical simulations have verified that the ICM can be substantially enriched during the peak of star formation at $2 < z < 3$ (e.g., Biffi et al. 2017, 2018a). Early AGN feedback may have played an essential role in displacing the metal-enriched gas produced within galaxies throughout the ICM (Truong et al. 2019).

We are able to constrain the metallicity profiles out to R_{200} for four galaxy groups, with temperatures of ~ 2.5 keV and with masses of an order of magnitude smaller than those of massive clusters. We found a nearly flat Fe abundance profile over the radii of $0.25-1.0 R_{200}$, as shown in Figure 1, with an average $Z_{\text{Fe}} = 0.309 \pm 0.018 Z_{\odot}$, which is remarkably similar to what is found in massive clusters. This $\text{Fe} \sim 0.3 Z_{\odot}$ uniform abundance distribution has also been found at the outskirts of two poor clusters, UGC 03957 (Thölken et al. 2016) and Virgo (Simionescu et al. 2015), whose peak temperatures are ~ 3.5 keV, which is between groups and clusters.

In addition to Fe, other elements (O, Mg, Si, S, and Ni) have nearly constant abundance throughout the outskirts of the groups, despite the larger uncertainties. Our findings are consistent with the same enrichment mechanism working among systems at various mass scales. Low mass systems form earlier than more massive systems in a hierarchical Universe. For metals to be deposited and well mixed before the gravitational collapse of galaxy groups, the timeline of the early-enrichment scenario, including the formation of SNIa (and their progenitor stars), needs to be pushed back further (e.g., Maoz et al. 2014; Biffi et al. 2018b).

5.2 Early enrichment population

A conundrum in the enrichment study is that the total metals observed in rich clusters cannot be explained by the visible stellar component, as shown in Figure 4 (also see E Blackwell et al. 2021; Ghizzardi et al. 2021). This discrepancy invokes an external and universal source of metals even *before* the star formation episode – an Early Enrichment Population (EEP), which is not visible today (Mantz et al. 2017). The time scale of this enrichment epoch is not well constrained, but possibly at $3 < z < 10$, and such an early stellar population may be directly observable with JWST.

Our findings demonstrate that once the Fe abundance is measured out to R_{200} , the current stellar content of galaxy groups is insufficient to produce their total metals. Nevertheless, within R_{500} and R_{200} , the effective Fe yields of groups are significantly smaller than those of rich clusters. In addition to Fe yields, this difference between groups and clusters is also reflected in their iron-mass-to-light ratios. As shown in Figure 3, we have derived the IMLR profiles of these groups out to R_{200} . Compared to the Perseus cluster, galaxy groups contain twice as much stellar light relative to their metal content. The small IMLRs of groups relative to clusters may be attributed to the relatively shallower potential wells of groups, making them unable to retain all the enriched gas against non-thermal processes such as AGN feedback. As shown in Sarkar et al. (2021a), the accumulated gas mass to total mass ratios within R_{200} are consistent with the cosmic baryon fraction for galaxy clusters, which are systematically higher than those of galaxy groups. Furthermore, groups and clusters may have different star formation histories. The IGrM has a lower temperature and density than the ICM, providing a less hostile environment for the member galaxies. The higher star formation rate

in galaxy groups may partially explain the small IMLR (Davé et al. 2008).

5.3 Chemical composition of galaxy groups

The additional constraints on O, Mg, Si, and S allow us to derive the chemical components and SNIa fraction of galaxy groups. The abundance ratios of O/Fe, S/Fe, Si/Fe, and Mg/Fe of the four groups in our sample are shown in Figure 2. Primarily caused by the abrupt change in the slope of the Fe abundance profile, we observe different chemical compositions between group centers and group outskirts. The X/Fe ratios within $0.25R_{200}$ are consistent with the Solar chemical composition, for which we derive a f_{SNIa} of 0.214 ± 0.028 . This is in agreement with the average gas abundance ratios of cluster cores (de Plaa et al. 2007) and 44 nearby systems within $R < R_{500}$ (dominated by galaxy clusters) in the CHEERS sample (Mernier et al. 2017). Similar chemical composition for gas has been found at the centers of the Perseus cluster using the microcalorimeter on board *Hitomi* (Simionescu et al. 2019), as well as in NGC 1404, an early-type galaxy, through a joint *XMM-Newton* EPIC, RGS, and *Chandra*-ACIS study (Mernier et al. 2022). It is intriguing that ICM, IGrM, and even ISM metallicities trace the same metal abundance pattern as our Solar System rather than their dominant galaxies. This further implies a common origin of the metals among these systems. Alternatively, this also means that the stellar population we see today in clusters and groups (i.e., mainly red-and-dead population) has very little to do with the metal content of their hot halos.

Over the radii of $0.25-1.0R_{200}$, the X/Fe ratios are generally super solar, ranging from 1.6 to 1.9, for which we derive that the SNIa fraction is 0.138 ± 0.046 , allowing us to rule out a pure SNcc enrichment by 3σ . The Fe abundance at the outskirts is unlikely to be significantly underestimated since we have employed a 2T model to mitigate the “Fe-bias”, and we have obtained a measured Z_{Fe} similar to that of the rich clusters. It is worth noting that the significant uncertainties and scatter of the measurements do not allow us to claim an apparent discrepancy from the solar value for S/Fe, Si/Fe, and Mg/Fe, while the O line can not be well resolved by CCD-like detectors such as XIS. An extensive *Suzaku* study of the outskirts of the Virgo cluster reveals a super solar value for Mg/Fe of $1.2-1.6$, while their Si/Fe and S/Fe ratios are $0.6-0.8$ and $0.8-1.2$, respectively. The X/Fe ratios may scatter among different systems. The results can be further complicated by the various sources of systematic effects associated with the observations of the background-dominated regimes.

6 SUMMARY

We analyzed joint *Suzaku* and *Chandra* observations of four nearby groups – MKW4, Antlia, RXJ1159+5531, and ESO3060170. *Suzaku* observations were used to constrain their gas properties, and *Chandra* data were used to refine the results by mitigating the uncertainties introduced by the CXB. We have derived abundance profiles of O, Mg, Si, S, Fe, and Ni out to the R_{200} for the first time for such low-mass systems. Our results are summarized below.

- The metal abundances in the central region of Antlia are significantly lower than those of MKW4, RXJ1159+5531, and

ESO3060170. Unlike the other three systems, Antlia is a non-cool-core group. As observed in massive system equivalents (i.e., non-cool-core clusters), more frequent merging events may have disrupted its core and erased much of the centrally peaked metallicity.

- At group outskirts ($0.25\text{-}1.0R_{200}$), we measure flat metal abundance profiles for all four groups, with an average Fe abundance of $Z_{\text{Fe}} = 0.309 \pm 0.018 Z_{\odot}$ ($\chi^2 = 14$ for 12 degrees of freedom), which is remarkably consistent with what was found in rich clusters, and predictions from IllustrisTNG for galaxy groups. The uniform metal distribution suggests that the same early enrichment process may have been at work before the gravitational collapse of groups and clusters. Early AGN feedback is likely to have played an essential role in transporting metals from galaxies to the hot gas as well as efficiently mixing the enriched gas throughout the proto cluster/group gas at $z = 2 - 3$. It is also plausible that an early-enrichment population is responsible for contaminating the proto cluster/group gas before the formation of the current stellar components at $3 < z < 10$.

- We derive the accumulated iron mass-to-light ratios from the center out to the R_{200} of these groups. Their IMLR profiles increase with radius, indicating that the enriched gas is more extended than the stellar distribution. Near R_{200} , the accumulated IMLR profiles of these groups are consistent with each other at $4\text{-}5 \times 10^{-3} M_{\odot}/L_{K\odot}$. However, these values are significantly lower than the accumulated IMLR of Perseus at R_{200} , which may imply that groups could not retain all of their enriched gas due to their shallower potential wells, and/or a halo-mass dependent star formation history.

- We compare the effective Fe yields of groups within R_{500} and R_{200} , and the theoretical expectation. The iron yields measured out to R_{200} of these four groups show tension with respect to the expected values from empirical supernovae yields, and in contrast with what can be observed within R_{500} . A significant amount of metals are found at the outskirts of groups. When the Fe abundance is measured out to R_{200} , the visible stellar component in the groups is insufficient to produce the observed metals, which may pose a challenge for the chemical enrichment models in the same fashion as the one already known for clusters.

- The O/Fe, Mg/Fe, Si/Fe, and S/Fe ratios at the group centers are nearly solar and consistent with the chemical composition measured at cluster centers. The hot gas in the systems that are orders of magnitude different in mass traces the same metal abundance pattern as our Solar System rather than their dominant galaxies. The derived SNIa fraction is 14% at their outskirts, allowing us to rule out a pure core collapsed supernovae enrichment before the gravitational collapse of galaxy groups.

ACKNOWLEDGEMENTS

We are grateful to Dan Maoz for the insightful comments that greatly helped to improve the paper. A. S. and Y. S. were supported by Chandra X-ray Observatory grant GO1-22126X, NASA grant 80NSSC21K0714, and NSF grant 2107711. SRON Netherlands Institute for Space Research is supported financially by NWO.

DATA AVAILABILITY

The data underlying this article will be shared on reasonable request to the corresponding author.

REFERENCES

- Asplund M., Grevesse N., Sauval A. J., Scott P., 2009, *ARA&A*, **47**, 481
- Badenes C., Borkowski K. J., Hughes J. P., Hwang U., Bravo E., 2006, *ApJ*, **645**, 1373
- Biffi V., et al., 2017, *MNRAS*, **468**, 531
- Biffi V., Mernier F., Medvedev P., 2018a, *Space Sci. Rev.*, **214**, 123
- Biffi V., Planelles S., Borgani S., Rasia E., Murante G., Fabjan D., Gaspari M., 2018b, *Monthly Notices of the Royal Astronomical Society*, **476**, 2689
- Böhringer H., Werner N., 2010, *A&ARv*, **18**, 127
- Buote D. A., 2000, *ApJ*, **539**, 172
- Buote D. A., Fabian A. C., 1998, *MNRAS*, **296**, 977
- Cash W., 1979, *ApJ*, **228**, 939
- Chakraborty P., Ferland G. J., Chatzikos M., Guzmán F., Su Y., 2020a, *ApJ*, **901**, 68
- Chakraborty P., Ferland G. J., Chatzikos M., Guzmán F., Su Y., 2020b, *ApJ*, **901**, 69
- Davé R., Oppenheimer B. D., Sivanandam S., 2008, *MNRAS*, **391**, 110
- Domainko W., et al., 2006, *A&A*, **452**, 795
- E Blackwell A., Bregman J. N., Snowden S. L., 2021, arXiv e-prints, p. arXiv:2105.04638
- Ettori S., Fabian A. C., 1999, *MNRAS*, **305**, 834
- Fabjan D., Borgani S., Tornatore L., Saro A., Murante G., Dolag K., 2010, *MNRAS*, **401**, 1670
- Freundlich J., Maoz D., 2021, *MNRAS*, **502**, 5882
- Gastaldello F., Simionescu A., Mernier F., Biffi V., Gaspari M., Sato K., Matsushita K., 2021, *Universe*, **7**, 208
- Ghizzardi S., De Grandi S., Molendi S., 2014, *A&A*, **570**, A117
- Ghizzardi S., et al., 2021, *A&A*, **646**, A92
- Gunn J. E., Gott J. Richard I., 1972, *ApJ*, **176**, 1
- Iwamoto K., Brachwitz F., Nomoto K., Kishimoto N., Umeda H., Hix W. R., Thielemann F.-K., 1999, *ApJS*, **125**, 439
- Koyama K., et al., 2007, *PASJ*, **59**, 23
- Leccardi A., Molendi S., 2008, *A&A*, **487**, 461
- Liu A., Tozzi P., Ettori S., De Grandi S., Gastaldello F., Rosati P., Norman C., 2020, *A&A*, **637**, A58
- Lovisari L., Reiprich T. H., 2019, *MNRAS*, **483**, 540
- Lovisari L., Reiprich T. H., Schellenberger G., 2015, *A&A*, **573**, A118
- Madau P., Dickinson M., 2014, *ARA&A*, **52**, 415
- Makishima K., et al., 2001, *PASJ*, **53**, 401
- Mantz A. B., Allen S. W., Morris R. G., Simionescu A., Urban O., Werner N., Zhuravleva I., 2017, *MNRAS*, **472**, 2877
- Maoz D., Graur O., 2017, *ApJ*, **848**, 25
- Maoz D., Mannucci F., Nelemans G., 2014, *ARA&A*, **52**, 107
- Marinacci F., et al., 2018, *MNRAS*, **480**, 5113
- Matsushita K., Böhringer H., Takahashi I., Ikebe Y., 2007, *A&A*, **462**, 953
- Matsushita K., Sato T., Sakuma E., Sato K., 2013, *PASJ*, **65**, 10
- McDonald M., et al., 2016, *ApJ*, **826**, 124
- McLaughlin D. E., 1999, *AJ*, **117**, 2398
- Mernier F., de Plaa J., Lovisari L., Pinto C., Zhang Y. Y., Kaastra J. S., Werner N., Simionescu A., 2015, *A&A*, **575**, A37
- Mernier F., de Plaa J., Pinto C., Kaastra J. S., Kosec P., Zhang Y. Y., Mao J., Werner N., 2016a, *A&A*, **592**, A157
- Mernier F., et al., 2016b, *A&A*, **595**, A126
- Mernier F., et al., 2017, *A&A*, **603**, A80
- Mernier F., et al., 2018a, *Space Sci. Rev.*, **214**, 129
- Mernier F., et al., 2018b, *MNRAS*, **478**, L116
- Mernier F., et al., 2022, arXiv e-prints, p. arXiv:2201.05161
- Million E. T., Werner N., Simionescu A., Allen S. W., 2011, *MNRAS*, **418**, 2744
- Murray C. E., Stanimirović S., Goss W. M., Heiles C., Dickey J. M., Babler B., Kim C.-G., 2018, *ApJS*, **238**, 14
- Naiman J. P., et al., 2018, *MNRAS*, **477**, 1206
- Nelson D., et al., 2018, *MNRAS*, **475**, 624
- Nomoto K., Tominaga N., Umeda H., Kobayashi C., Maeda K., 2006, *Nuclear Phys. A*, **777**, 424
- Nomoto K., Kobayashi C., Tominaga N., 2013, *ARA&A*, **51**, 457

- Nulsen P. E. J., Böhringer H., 1995, *Monthly Notices of the Royal Astronomical Society*, 274, 1093
- Pillepich A., et al., 2018, *MNRAS*, 475, 648
- Planelles S., Borgani S., Fabjan D., Killeddar M., Murante G., Granato G. L., Ragone-Figueroa C., Dolag K., 2014, *MNRAS*, 438, 195
- Rasmussen J., Ponman T. J., 2007, *MNRAS*, 380, 1554
- Rasmussen J., Ponman T. J., 2009, *MNRAS*, 399, 239
- Renzini A., Andreon S., 2014, *MNRAS*, 444, 3581
- Salpeter E. E., 1955, *ApJ*, 121, 161
- Sarkar A., Su Y., Randall S., Gastaldello F., Trierweiler I., White R., Kraft R., Miller E., 2021a, *MNRAS*, 501, 3767
- Sarkar A., et al., 2021b, *ApJ*, 907, 12
- Sasaki T., Matsushita K., Sato K., 2014, *ApJ*, 781, 36
- Sato K., Matsushita K., Gastaldello F., 2009, *PASJ*, 61, S365
- Simionescu A., Werner N., Böhringer H., Kaastra J. S., Finoguenov A., Brüggén M., Nulsen P. E. J., 2009, *A&A*, 493, 409
- Simionescu A., et al., 2011, *Science*, 331, 1576
- Simionescu A., Werner N., Urban O., Allen S. W., Ichinohe Y., Zhuravleva I., 2015, *ApJ*, 811, L25
- Simionescu A., et al., 2019, *MNRAS*, 483, 1701
- Springel V., et al., 2018, *MNRAS*, 475, 676
- Su Y., White Raymond E. I., Miller E. D., 2013, *ApJ*, 775, 89
- Su Y., Buote D., Gastaldello F., Brighenti F., 2015, *ApJ*, 805, 104
- Sukhbold T., Ertl T., Woosley S. E., Brown J. M., Janka H. T., 2016, *ApJ*, 821, 38
- Thölken S., Lovisari L., Reiprich T. H., Hasenbusch J., 2016, *A&A*, 592, A37
- Truong N., et al., 2019, *MNRAS*, 484, 2896
- Tsujimoto T., Nomoto K., Yoshii Y., Hashimoto M., Yanagida S., Thielemann F. K., 1995, *MNRAS*, 277, 945
- Urban O., Werner N., Allen S. W., Simionescu A., Mantz A., 2017, *MNRAS*, 470, 4583
- Werner N., de Plaa J., Kaastra J. S., Vink J., Bleeker J. A. M., Tamura T., Peterson J. R., Verbunt F., 2006, *A&A*, 449, 475
- Werner N., Urban O., Simionescu A., Allen S. W., 2013, *Nature*, 502, 656
- Wiersma R. P. C., Schaye J., Theuns T., Dalla Vecchia C., Tornatore L., 2009, *MNRAS*, 399, 574
- Wong K.-W., Irwin J. A., Wik D. R., Sun M., Sarazin C. L., Fujita Y., Reiprich T. H., 2016, *ApJ*, 829, 49
- de Grandi S., Molendi S., 2009, *A&A*, 508, 565
- de Plaa J., Werner N., Bleeker J. A. M., Vink J., Kaastra J. S., Méndez M., 2007, *A&A*, 465, 345

This paper has been typeset from a $\text{\TeX}/\text{\LaTeX}$ file prepared by the author.

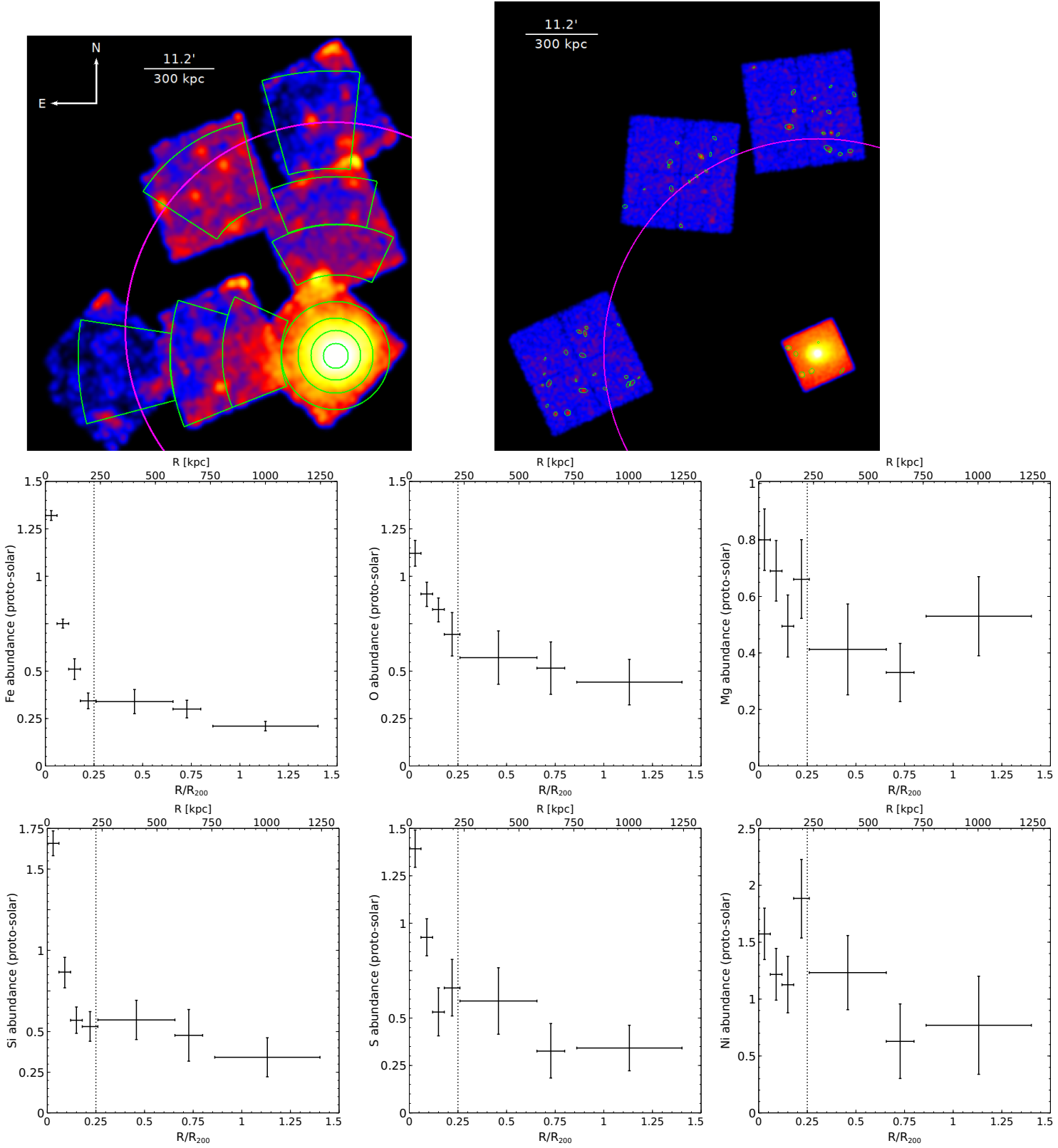


Figure A1. Top left: NXB subtracted and exposure corrected mosaic *Suzaku* image of MWK4 in the 0.5-2 keV energy band. Magenta circle indicates R_{200} . Green annuli represent the regions used for spectra extraction. Top right: mosaic *Chandra* image of MKW4 in the 0.5-7.0 keV energy band. The resolved point sources are marked in green elliptical regions. Middle and Bottom: radial profiles of different elements from the group center to the outskirts. Vertical dotted line indicate $0.25R_{200}$.

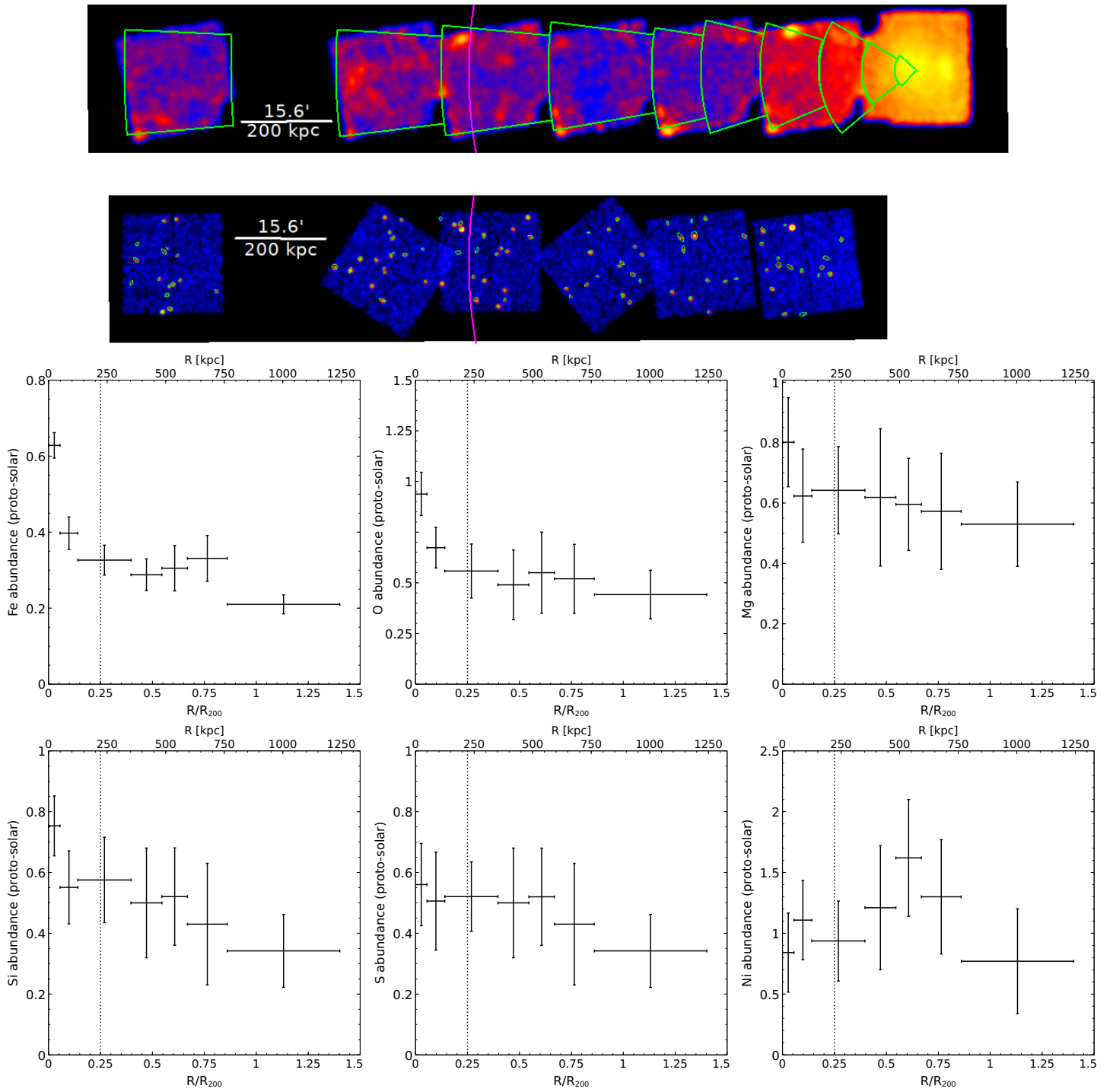


Figure A2. Antlia; same as Figure A1.

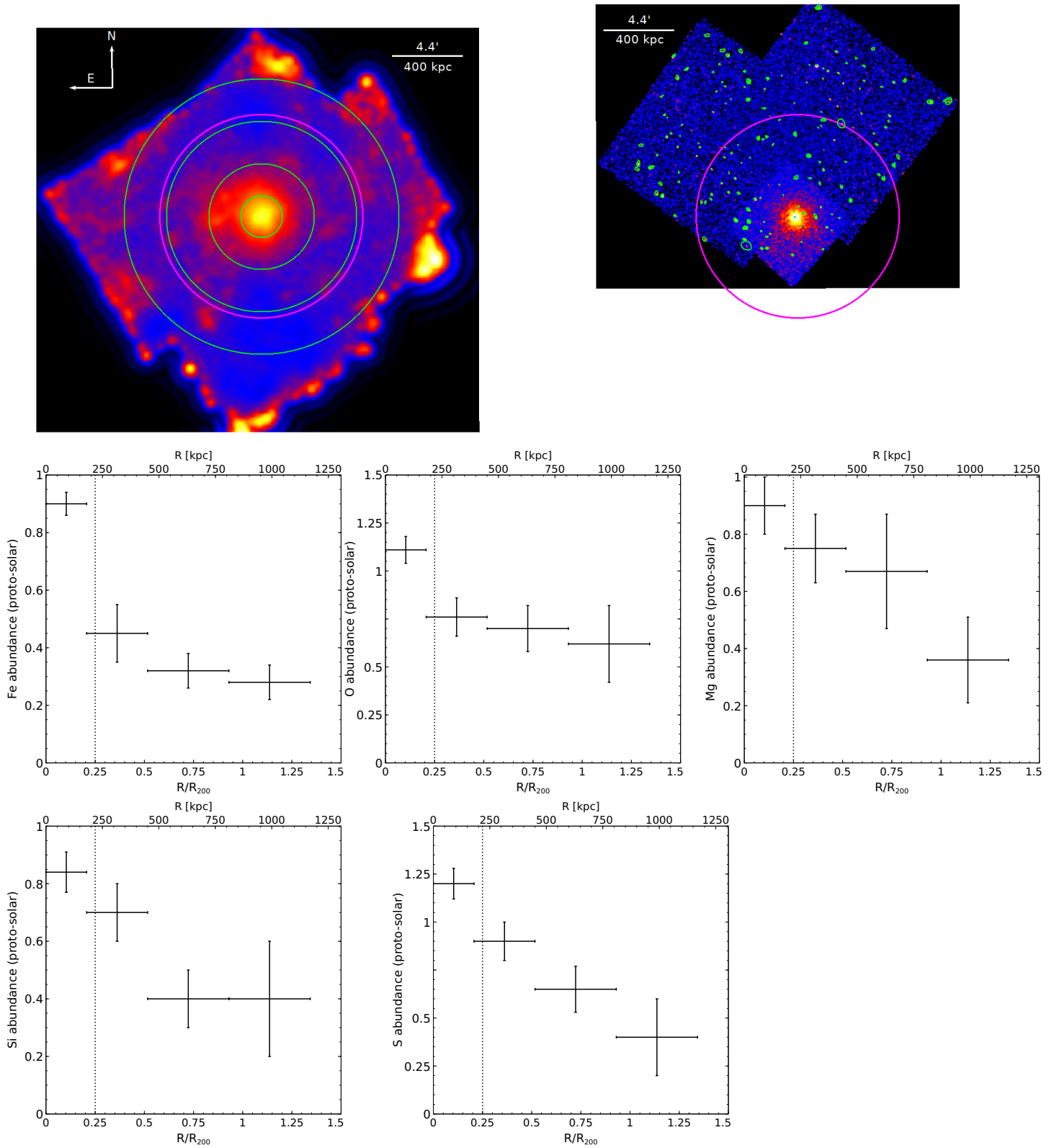


Figure A3. RXJ 1159; same as Figure A1.

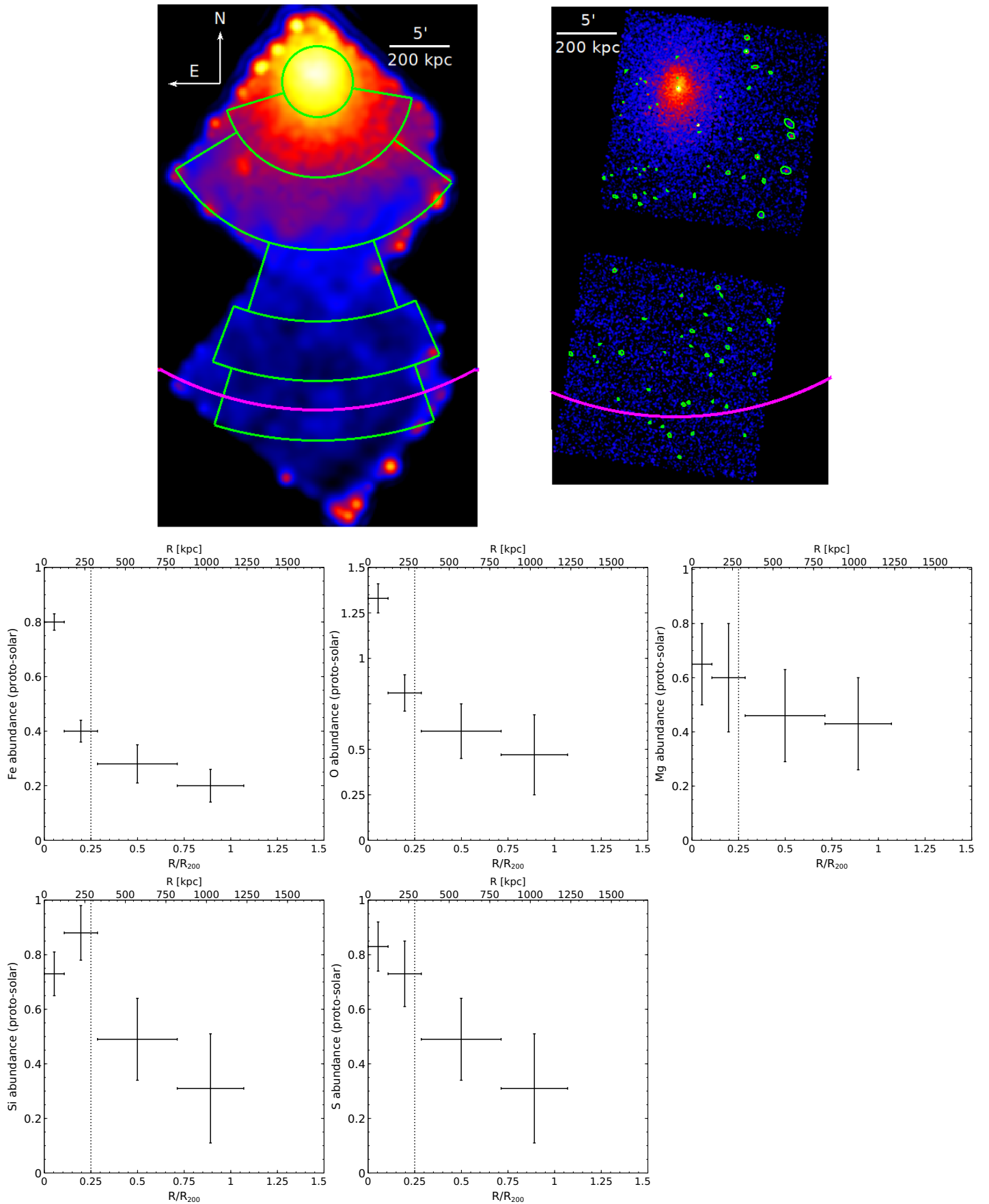


Figure A4. ESO 3060170; same as Figure A1

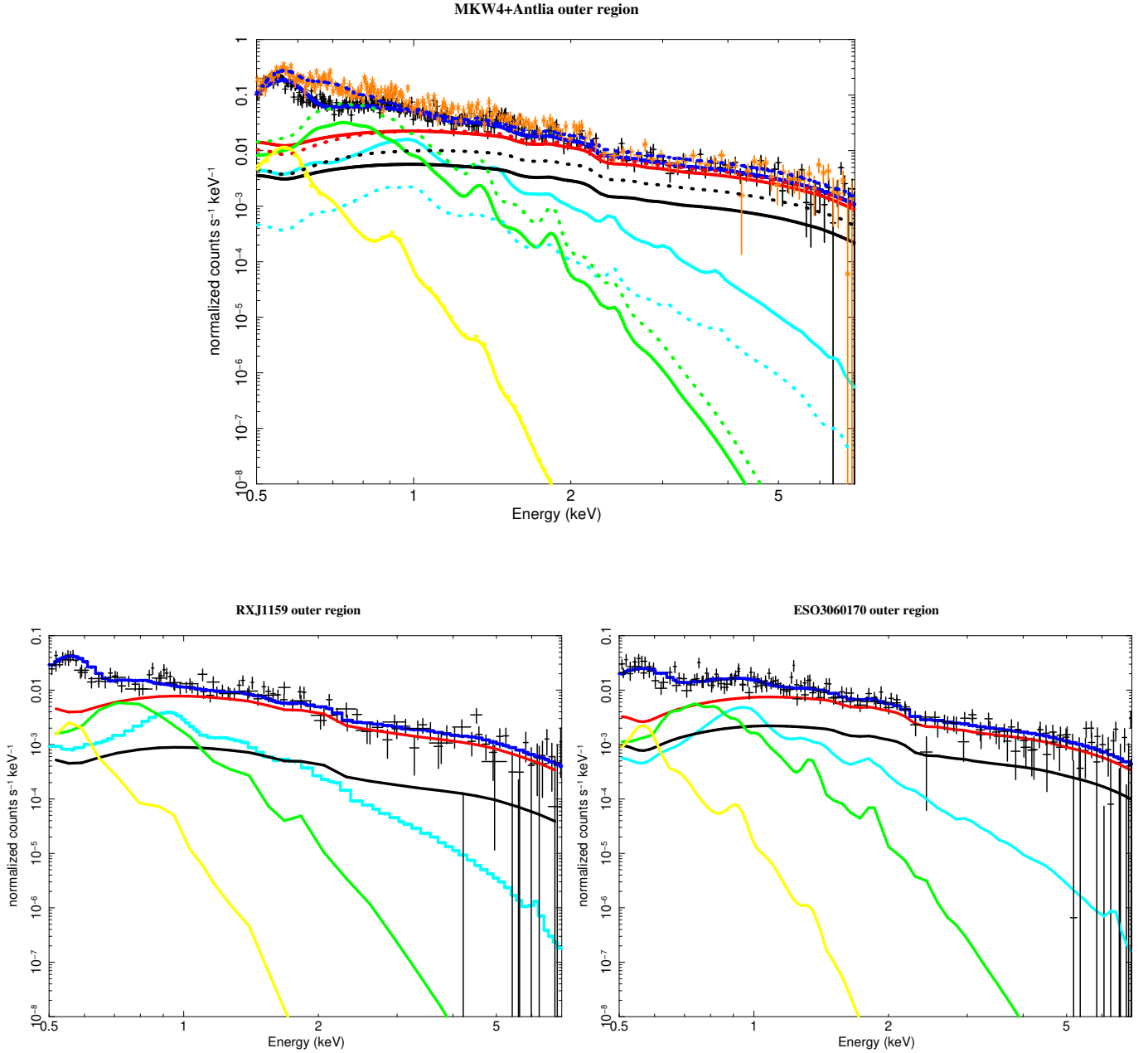


Figure A5. Best-fit results of the spectral analysis for the outermost regions of four groups. We show only XIS1 spectra. Red, black, cyan, green, yellow colored lines indicate best-fit resolved CXB, unresolved CXB, ICM emission, GH, LHB components, respectively. Blue line shows the best-fit ICM emission and X-ray background together. *Top panel:* Black data points are for MKW4. Orange data points are for Antlia. Solid line represents MKW4 and dashed line represents Antlia. *Bottom panel:* spectra for RXJ1159 and ESO3060170.